Proceedings of FEDSM '99
3rd ASME/JSME Joint Fluids Engineering Conference
July 18-23, 1999, San Francisco, California

FEDSM99-7364

MULTI-PHASE CFD ANALYSIS OF NATURAL AND VENTILATED CAVITATION ABOUT SUBMERGED BODIES

Robert F. Kunz **David A. Boger**
Thomas S. Chyczewski
David R. Stinebring **Howard J. Gibeling**
Penn State Applied Research Laboratory
University Park, Pennsylvania 16802
814-865-2144, rfk102@psu.edu

T.R. Govindan
NASA Ames Research Center
Moffett Field, California 94035

ABSTRACT

A multi-phase CFD method has been developed and is applied here to model the flow about submerged bodies subject to natural and ventilated cavitation. The method employs an implicit, dual-time, pre-conditioned, multi-phase Navier-Stokes algorithm and is three-dimensional, multi-block and parallel. It incorporates mixture volume and constituent volume fraction transport/generation for liquid, condensable vapor and non-condensable gas fields. Mixture momentum and turbulence scalar equations are also solved. Mass transfer modeling provides exchange between liquid and vapor phases. The model accounts for buoyancy effects and the presence/interaction of condensable and non-condensable fields.

In this paper, the theoretical formulation of the method is summarized. Results are presented for steady-state and transient axisymmetric flows with natural and ventilated cavitation about several bodies. Comparisons are made with available measurements of surface pressure distribution, cavitation bubble geometry and drag coefficient. Three-dimensional results are presented for a submerged body running at several angles of attack. The underlying three-species formulation and the specific models employed for mass transfer and momentum diffusion are demonstrated to provide good correspondence with measurements; however, several weaknesses in the current modeling are identified and discussed.

INTRODUCTION

Cavitation can occur in a wide range of liquid flows, including those through rotating machinery and nozzles and about underwater bodies. In these applications, the proximity of local pressure to the vapor pressure of the liquid can give rise to cavitation. The physics of the resulting two-phase flow are highly complex and remain only partially understood. Cavitation is usually associated with negative design implications, including structural damage, noise and lost loading. Alternatively, drag reduction can be realized if bodies are partially or fully enveloped in a large natural or ventilated gas cavity. This latter application motivates the present effort.

Natural and ventilated cavities about submerged bodies and turbomachinery blades are characteristically unsteady but may define a "fixed" cavitation bubble or sheet in a time-average sense. Such sheet cavitation has been studied for decades and recently has become the target of CFD practitioners.

Early efforts to model sheet cavities relied on potential flow methods for the fluid flow outside the bubble, while the shape and size of the bubble itself were determined from dynamic equilibrium assumptions across the bubble-liquid interface and generally ad-hoc specification of bubble shape family and/or closure conditions. These "interface tracking" methods have been deployed for years but retain the limitations of a potential flow model applied to a flow with inherently vortical structures such as reentrant jets and trailing vortices.

A hierarchy of more modern viscous CFD methods have recently been brought to bear in modeling sheet cavitation. In one class of methods, a single continuity equation is considered with the density varying abruptly between vapor and liquid densities. An equation of state provides the local density, which is a strong function of proximity of the local pressure to vapor pressure (Song and He [1998], Chen and Heister [1994], for example). Though these methods can directly model viscous effects, they are inherently unable to distinguish between condensable vapor and non-condensable gas, a requirement of our current application.

By solving separate continuity equations for liquid and gas phase fields, one can account for and model the separate dynamics and thermodynamics of the liquid, condensable vapor, and non-condensable gas fields. Merkle et. al. [1998] have deployed such a two-species formulation in the analysis of natural sheet cavitation. This is the level of modeling employed here,

though a three-species formulation is employed to account for two gaseous fields.

Full-two-fluid modeling, wherein separate momentum (and in principle energy) equations are employed for the liquid and vapor constituents have also been utilized for natural cavitation (Grogger and Alajbegovic [1998]) in a venturi analysis. The gas-liquid interface in sheet cavity flows are known to be close to dynamic equilibrium, so for our present interests, we choose not to pursue the full-two-fluid level of modeling.

Our principal interest is in analyzing flows about vehicles with running cavitation. In cavity running bodies, much of the configuration is enveloped in a gas cavity. In general, this gas cavity is composed of a mixture of water vapor and ventilated gases. Sharp fore-body or *cavitator* curvatures, as well as injection of large quantities of gases, can stabilize sheet cavities. The former tends to "anchor" cavitation inception, while the latter can reduce or eliminate the characteristic unsteadiness ("re-entrant jet") in the bubble closure region. Still, many relevant applications exhibit large scale unsteadiness associated with re-entrant jets, periodic ejection of non-condensable gas and cavity "pulsations". Accordingly, we retain here a time-accurate formulation.

The success of this approach is, of course, dependent on the ability to obtain converged steady or time accurate solutions for configurations of interest and to demonstrate validation of the method against available experimental data. In this spirit, what follows demonstrates the effectiveness and shortcomings of this method applied to natural and vented cavities about a variety of two-dimensional and three-dimensional configurations.

The paper is organized as follows: The theoretical formulation of the method is summarized, including baseline differential model, specific physical models and numerical methods. This is followed by three sets of results. First, naturally cavitating flows about three axisymmetric configurations are analyzed across a range of cavitation numbers, and these results are compared to experimental measurements. Next, an axisymmetric ventilated configuration is analyzed and compared to corresponding natural cavities at a range of cavitation numbers. Lastly, the three-dimensional capability of the method is demonstrated by analyzing natural cavitation about a cylindrical after-body with a hemispherical fore-body at several angles of attack. The capabilities and shortcomings of the method are assessed from these results.

NOMENCLATURE

Symbols

C_1, C_2	turbulence model constants
C_{dest}, C_{prod}	mass transfer model constants
C_P	pressure coefficient
C_D	drag coefficient
d	body diameter
d_m	bubble diameter
g_i	gravity vector
k	turbulent kinetic energy
L	bubble length
$\dot{m}^-$, $\dot{m}^+$	mass transfer rates
P	turbulent kinetic energy production
Pr_{tk},$Pr_{t\varepsilon}$	turbulent Prandtl numbers for k and ε
p	pressure
Re	Reynolds number
s	arc length along configuration
t, t_∞	time, mean flow time scale (d/U_∞)
U	velocity magnitude
u_i	Cartesian velocity components
x_i	Cartesian coordinates
α	volume fraction, angle of attack
β	preconditioning parameter
ε	turbulence dissipation rate
μ	molecular viscosity
ρ	density
σ	cavitation number ($\equiv \frac{p_\infty - p_v}{1/2\rho_l U_\infty^2}$)

Subscripts, Superscripts

l	liquid
m	mixture
ng	non-condensable gas
t	turbulent
v	condensable vapor
∞	free stream value

THEORETICAL FORMULATION

Governing Equations and Physical Modeling

A three species differential formulation is adopted where individual equations are provided for the transport/generation of volume fraction of liquid (which can exchange mass with condensable vapor), volume fraction of non-condensable gas and the mixture volume. A mixture momentum equation is also provided. The governing differential equations cast in Cartesian tensor form are given as:

$$\left(\frac{1}{\rho_m\beta^2}\right)\frac{\partial p}{\partial \tau}+\frac{\partial u_j}{\partial x_j} = (\dot{m}^+ + \dot{m}^-)\left(\frac{1}{\rho_l}-\frac{1}{\rho_v}\right)$$

$$\frac{\partial}{\partial t}(\rho_m u_i)+\frac{\partial}{\partial \tau}(\rho_m u_i)+\frac{\partial}{\partial x_j}(\rho_m u_i u_j) = -\frac{\partial p}{\partial x_i}+\frac{\partial}{\partial x_j}\left(\mu_{m,t}\frac{\partial u_i}{\partial x_j}\right)+\rho_m g_i \quad (1)$$

$$\frac{\partial \alpha_l}{\partial t}+\left(\frac{\alpha_l}{\rho_m\beta^2}\right)\frac{\partial p}{\partial \tau}+\frac{\partial \alpha_l}{\partial \tau}+\frac{\partial}{\partial x_j}(\alpha_l u_j) = \left(\frac{\dot{m}^+}{\rho_l}+\frac{\dot{m}^-}{\rho_l}\right)$$

$$\frac{\partial \alpha_{ng}}{\partial t}+\left(\frac{\alpha_{ng}}{\rho_m\beta^2}\right)\frac{\partial p}{\partial \tau}+\frac{\partial \alpha_{ng}}{\partial \tau}+\frac{\partial}{\partial x_j}(\alpha_{ng} u_j) = 0$$

where mixture density and turbulent viscosity are defined from:

$$\rho_m = \rho_l\alpha_l + \rho_v\alpha_v + \rho_{ng}\alpha_{ng}$$
$$\mu_{m,t} = \frac{\rho_m C_\mu k^2}{\varepsilon} \quad (2)$$

In the present work, the density of each constituent is taken as constant. Equations 1 represent transport/generation of mixture volume, mixture momentum, liquid phase volume fraction and non-condensable gas volume fraction, respectively. Physical time derivatives are included for transient computations. The formulation incorporates pre-conditioned *pseudo*-time-derivatives ($\partial/\partial\tau$ terms), defined by parameter β, which provide favorable convergence characteristics for steady state and transient computations, as discussed further below.

The formation and collapse of a cavity is modeled as a phase transformation. Detailed modeling of this process requires knowledge of the thermodynamic behavior of the fluid near a phase transition point and the formation of interfaces. One approach is the use of the Ginzburg-Landau potential (Hohenberg and Halperin [1977], for example). Such an approach is being pursued (last author) but is not yet complete. Related behavior can also be described by van der Waals' equation of state. Simplified models based on the more detailed approach are presented here. Simplifications result from the use of empirical factors. Two separate models are used to describe the transformation of liquid to vapor and the transformation of vapor back to liquid. For transformation of liquid to vapor, $\dot{m}^-$ is modeled as being proportional to the liquid volume fraction and the amount by which the pressure is below the vapor pressure. This model is similar to that used by Merkle et. al. [1998] for both evaporation and condensation. For transformation of vapor to liquid, a simplified form of the Ginzburg-Landau potential is used for the mass transfer rate $\dot{m}^+$.

$$\dot{m}^- = \frac{C_{dest}\rho_l\alpha_l \mathrm{MIN}[0, p - p_v]}{(1/2\rho_l U_\infty^2)t_\infty}$$
$$\dot{m}^+ = \frac{C_{prod}\rho_l\alpha_l^2(1-\alpha_l)}{t_\infty} \quad (3)$$

C_{dest} and C_{prod} are empirical constants (here $C_{dest} = 0.2$, $C_{prod} = 0.2$). Both mass transfer rates are non-dimensionalized with respect to a mean flow time scale.

In this work a high Reynolds number form k-ε model with standard wall functions is implemented to provide turbulence closure:

$$\frac{\partial}{\partial t}(\rho_m k) + \frac{\partial}{\partial x_j}(\rho_m k u_j) = \frac{\partial}{\partial x_j}\left(\frac{\mu_{m,t}}{Pr_{tk}}\frac{\partial k}{\partial x_j}\right) + P - \rho\varepsilon$$
$$\frac{\partial}{\partial t}(\rho_m \varepsilon) + \frac{\partial}{\partial x_j}(\rho_m \varepsilon u_j) = \frac{\partial}{\partial x_j}\left(\frac{\mu_{m,t}}{Pr_{t\varepsilon}}\frac{\partial \varepsilon}{\partial x_j}\right) + [C_1 P - C_2\rho\varepsilon]\left(\frac{\varepsilon}{k}\right) \quad (4)$$

As with velocity, the turbulence scalars are interpreted as being mixture quantities.

In the present work, the effect of surface tension is not incorporated, since interface curvatures are very small for the configurations considered.

Numerical Method

The baseline numerical method is evolved from the work of Taylor and his coworkers at Mississippi State University (Taylor et. al. [1995], for example). The UNCLE code which served as the baseline platform for the present work, is based on a single phase, pseudocompressibility formulation. Third-order Roe-based flux difference splitting is utilized for convection term discretization. An implicit procedure is adopted with inviscid and viscous flux Jacobians approximated numerically. A block-symmetric Gauss-Siedel iteration is employed to solve the approximate Newton system at each timestep.

The multi-phase extension of the code retains these underlying numerics but incorporates two additional volume fraction constituent transport equations. A non-diagonal *pseudo*-time-derivative preconditioning matrix is also employed which ameliorates the stiffness associated with the vanishing time derivative term in the mixture continuity equation as the limit of incompressible constituent phases is approached. This preconditioner gives rise to a system with well-conditioned eigenvalues which are independent of density ratio and local volume fraction. This system is well suited to high density ratio, phase-separated two-phase flows, such as the cavitating systems of interest here.

A temporally second-order accurate dual-time scheme was implemented for physical transients. The turbulence transport equations are solved subsequent to the mean flow equations at each time step. The multiblock code is instrumented with MPI for parallel execution based on domain decomposition. Further details on the numerical method and code are available in Kunz et. al. [1999].

RESULTS

Three sets of results are presented in this section. First, results are presented for axisymmetric flows over several cylindrical bodies with different cavitator shapes. Hemispherical, blunt cylindrical and conical nose shapes were studied across a range of cavitation numbers. The second set of results are for ventilated cavitating flow over a blunt cylindrical body with gas injection near the leading edge. The third set of results are three-dimensional simulations of natural cavitation about a cylindrical after-body with a hemispherical fore-body.

Natural Cavitation on Axisymmetric Bodies

Rouse and McNown [1948] carried out a series of experiments on natural cavitation about axisymmetric configurations. These each had cylindrical afterbodies with a flow-aligned axis and either conical, ogival or blunt fore-body or *cavitator* shapes. At low cavitation numbers, these flows exhibit natural cavitation initiating near or just aft of the intersection between the fore-body and the cylindrical body. For each configuration, measurements were made across a range of cavitation numbers, including a single phase case (large σ). Surface static pressure measurements were taken along the cavitator and after-body. Photographs were also taken from which approximate bubble size and shape

were deduced.

Several of the Rouse-McNown configurations were computed here. These included hemispherical (0.5 caliber ogive), blunt (0.0 caliber ogive) and conical (22.5^o cone half-angle) cavitator shapes. The experiments were performed at Reynolds numbers greater than 100,000 based on maximum cavitator (i.e., after-body) diameter. A value of Re = 136000 was used for the simulations. A range of grid sizes was used. For the hemispherical and conical configurations, grid sizes of 65x17, 129x33 and 257x65 were run. Figure 1 demonstrates that differences between predicted surface pressures for the medium and fine meshes are small. The fine meshes were used for all subsequent calculations presented here. For the blunt fore-body, a two-block grid topology had to be used, and a mesh consistent with the resolution and clustering of the other head-forms was utilized (65x49, 257x65 for blocks 1 and 2; see Figure 3c).

Figures 2a-c show comparisons between predicted and measured surface pressure distributions for the three configurations at a range of cavitation numbers. For all cases, as the cavitation number is decreased from near a critical "inception" value, a cavitation bubble forms and grows. The presence of the bubble manifests itself as a decrease in magnitude, flattening and lengthening of the pressure minimum along the surface. Also, bubble closure gives rise to an overshoot in pressure recovery due to the local stagnation associated with free-stream liquid flowing over the convex curvature at the aft end of the bubble. In Figure 2a, it is observed that for the hemispherical head-form, the method accurately captures the pressure distribution on the configuration across the range of cavitation numbers for which measurements were made. In Figure 3a, surface pressure contours, field liquid volume fraction contours, selected streamlines and the grid are illustrated for the $\sigma = 0.3$ case. A discrete bubble shape is observed. The aft end of the predicted bubble does not exhibit a smooth "ellipsoidal" closure. Indeed, due to local flow reversal (reentrant jet), liquid is swept back underneath the vapor pocket. The pressure in this region retains the nearly constant freestream liquid flow value impressed through the bubble. Similar closure region observations have been made by Chen and Heister [1994].

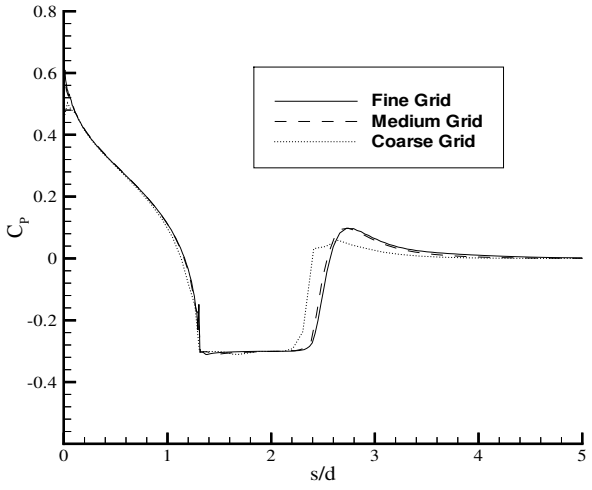

Figure 1. Comparison of predicted surface pressure distributions for naturally cavitating axisymmetric flow over a conical cavitator-cylindrical after-body configuration, $\sigma = 0.3$. Coarse (65x17), medium (129x33) and fine (257x65) mesh solutions are plotted.

Figures 2b and 3b provide corresponding results for a conical fore-body shape with a 22.5^o half-angle. Here, the simulation underpredicts the length of the bubble at all cavitation numbers, but qualitative trends remain correctly predicted.

Results for a blunt fore-body are presented in Figures 2c and 3c. Though good quantitative agreement is obtained at low cavitation numbers, two shortcomings of the present modeling are evident. First, even the single phase pressure distribution shows significant discrepancy from the data. In particular, the characteristic flattening of the measured pressure distribution due to a large recirculation zone aft of the corner is significantly underpredicted. Such a "forward facing step" flow is well known to provide significant challenges to single phase turbulence models. The conventional model employed here (high Reynolds number k-ε) has well-documented difficulties with stagnated, high strain and recirculating flows. All of these characteristics are embodied in the blunt head-form flow. Our efforts to "remedy" these single phase turbulence modeling shortcomings by deploying several approaches which have appeared in the literature remain incomplete and are beyond the scope of the present paper.

The second modeling shortcoming evident in the blunt head-form results is associated with the slight underprediction of cavity pressure at intermediate cavitation numbers. Indeed, the analysis predicts a large cavity at nearly constant pressure (vapor pressure) which initiates very close to the leading edge. The data exhibits a higher surface pressure near the leading edge, which approaches the vapor pressure with increased distance from the leading edge. This phenomenon arises due to the presence of a pressure minimum away from the body at the core of the strong vorticity associated with the leading edge separation. Physically, this is where cavitation initiates in this flow. The growth, interaction and transport of the small cavitation nuclei then give rise to a larger cavitation bubble emanating from this off-body location. The current modeling is unable to capture these relevant physics, though local pressure minimums are predicted to occur off-body aft of the leading edge. Attempts to adjust the time constant in Equation 3 (C_{dest}/t_∞) have proved unsuccessful, so this remains an ongoing modeling challenge.

Several parameters of relevance in the characterization of cavitation bubbles include body diameter, d, bubble length, L, bubble diameter, d_m, and form drag coefficient associated with the cavitator, C_D. Some ambiguity is inherent in both the experimental and computational definition of the latter three of these parameters. Bubble closure location is difficult to define due to unsteadiness and its dependence on after-body diameter (which can range from 0 [isolated cavitator] to the cavitator diameter). Accordingly, bubble length is often, and here, taken as twice the distance from cavity leading edge to the location of maximum bubble diameter (see Figure 4). The form drag coefficient is taken as the pressure drag on an isolated cavitator shape. For cavitators with afterbodies, such as here, the pressure contribution to C_D associated with the back of the cavitator is assumed equal to the cavity pressure ($\cong p_v$). For the simulations, d_m is determined by examining the $\alpha_l = 0.5$ contour and determining its maximum radial location.

In Figure 5a, the quantity $L/(dC_D^{1/2})$ is plotted against cavitation number for a large number of experimental data sets assembled by May [1975] from a variety of sources and for sixteen simulations made with the three cavitator shapes under con-

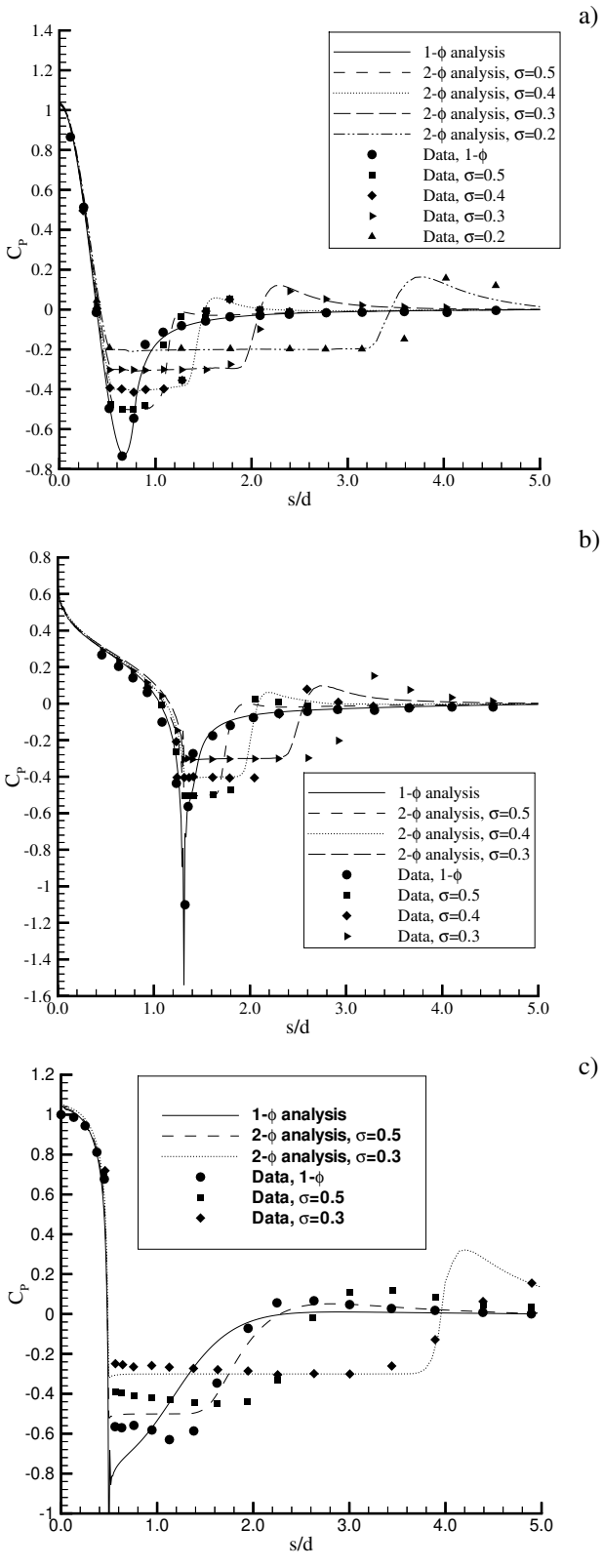

Figure 2. Comparison of predicted and measured surface pressure distributions at several cavitation numbers. a) hemispherical fore-body, b) conical fore-body, c) blunt fore-body.

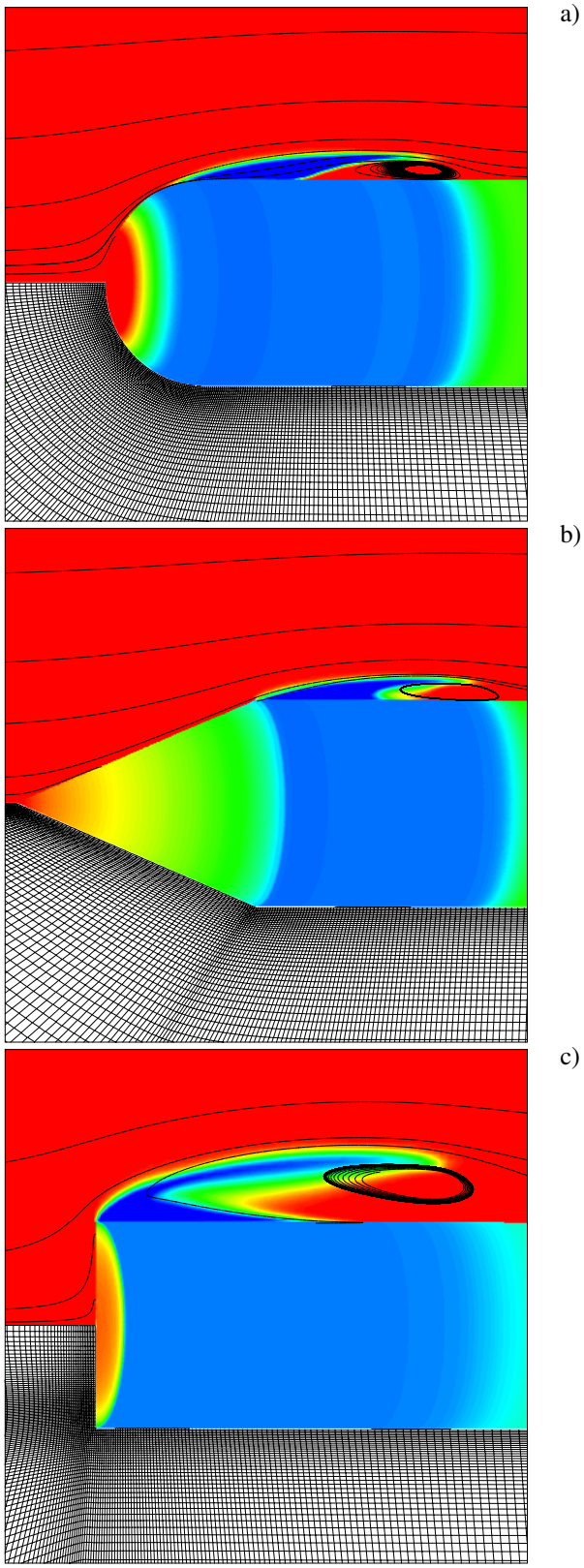

Figure 3. Predicted liquid volume fraction and surface pressure contours, selected streamlines and computational grid. a) hemispherical fore-body (σ=0.3), b) conical fore-body (σ=0.3), c) blunt fore-body (σ=0.4).

sideration here. That $L/(dC_D^{1/2})$ should correlate with σ has been long established theoretically and experimentally (Reichardt [1946], Garabedian [1956], for example). Despite the significant uncertainties associated with experimental and computational evaluation of L and C_D, the data and simulations do correlate well, close to independently of cavitator shape. The cone shaped cavitator exhibits some underprediction of this parameter at higher cavitation numbers, consistent with the bubble length underprediction observed in the pressure distribution comparisons presented above.

The so-called *fineness ratio* of the cavity, L/d_m, is plotted against cavitation number in Figure 5b for the same experimental and computational data sets. These parameters again correlate well for both experiment and simulation, though at higher cavitation numbers there is a spread in both. Considering the difficulties in quantifying smaller bubble sizes, we hesitate to draw any conclusions as to the possible sources of this spread.

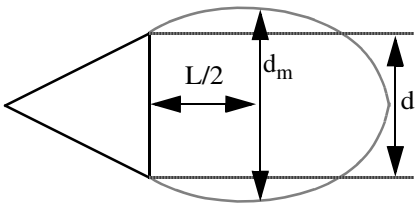

Figure 4. Bubble length and bubble diameter definitions.

In the cases considered so far, steady-state solutions were obtained for higher cavitation numbers. At lower cavitation numbers (i.e. larger bubbles), significant large scale unsteadiness appears in the aft region of the bubble/reentrant jet region. Vorticity and condensable vapor are shed from this region. Accordingly, transient simulations (dual-time stepping) were performed when pseudo-timestepping failed to converge. For the hemispherical, conical and blunt cavitator shapes, transient computations were performed for cavitation numbers less than or equal to $\sigma = 0.2$, 0.2 and 0.4, respectively. Non-dimensional physical time steps of $\Delta t/t_\infty = 0.007$ were utilized here.

In Figures 5a and 5b, time accurate CFD results are represented with filled symbols, steady state results with open symbols. In the transient simulations, drag and bubble geometry parameters are obtained as mean values from a sufficiently long transient record. For example, Figure 6 shows the 2000 timestep history of drag coefficient for the hemispherical cavitator simulation at $\sigma = 0.05$ (average $C_D = 0.309$).

Ventilated Cavitation

Ventilated cavities are also of interest to the authors because for large enough values of freestream pressure the only way to generate large cavities is to inject some mixture of condensable and non-condensable gases into the flow near the body leading edge. In general, ventilated cavities exhibit similar dynamics to natural cavities (May [1975]). Ventilated cavities do, however, tend to be more stable than natural cavities near the aft end of the cavitation bubble. Also, all non-condensable gas must mix with the freestream liquid and be transported downstream.

The axisymmetric blunt fore-body configuration presented above was run with no mass transfer but with non-condensable gas injection just aft of the leading edge. A range of injection mass flow rates were specified, yielding a range of ventilated cavity sizes. The resulting cavities do not close in the sense that all vapor is condensed, however a distinct bubble shape is observed whose geometry is quantified as detailed above. This is illustrated in Figure 7, where the predicted liquid

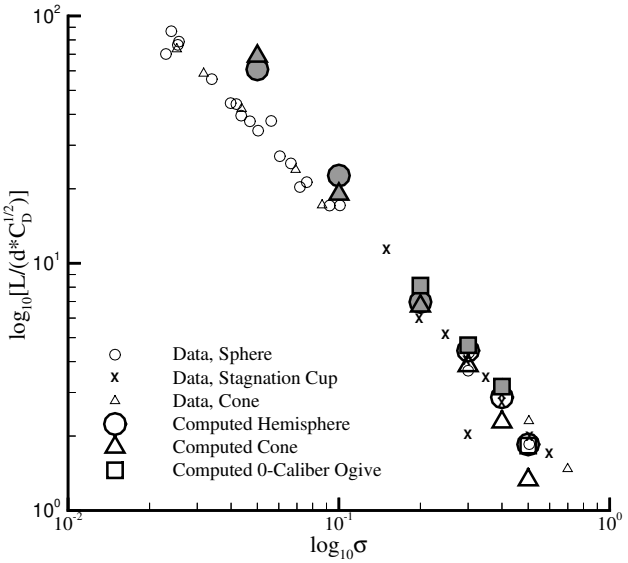

Figure 5a. Comparison of $L/(dC_D^{1/2})$ vs. σ for numerous fore-body shapes. Experimental data adapted from May [1975]. Open symbols represent steady computations, filled symbols represent transient computations.

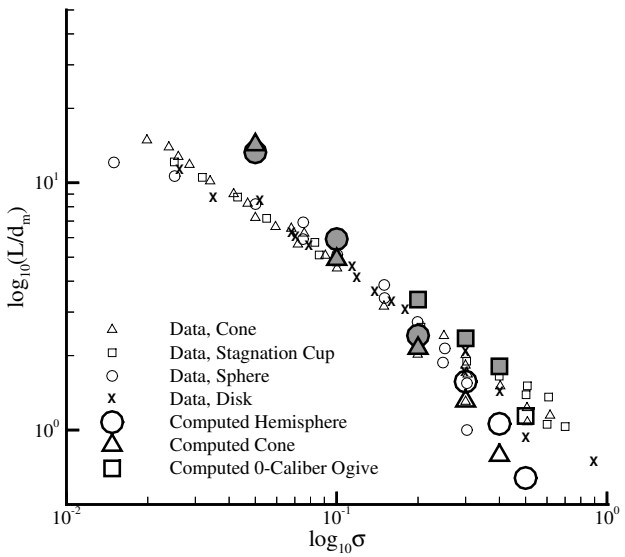

Figure 5b. Comparison of L/d_m vs. σ for numerous fore-body shapes. Experimental data adapted from May [1975]. Open symbols represent steady computations, filled symbols represent transient computations.

volume fraction fields are shown for the blunt head-form natural and vented cavities at $\sigma = 0.4$. (The cavitation number in ventilated cavities is defined not from the vapor pressure but from the cavity pressure.)

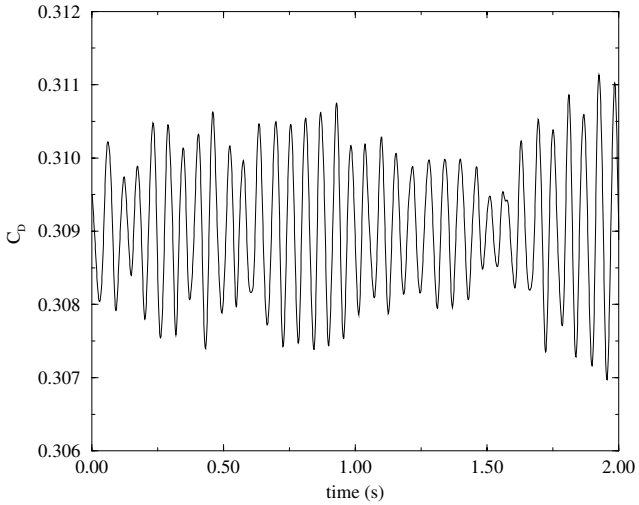

Figure 6. Predicted drag coefficient for the 2000 time step transient simulation of a cylindrical configuration with hemispherical fore-body at $\sigma = 0.05$.

In Figures 8a and 8b, $L/(dC_D^{1/2})$ and L/d_m are plotted for the blunt head-form at a range of cavitation numbers. The natural cavity results presented above are reproduced in these plots along with the results of six ventilated cavity runs. (Note that the cavitation number is not explicitly specified in the ventilated case; rather it is an outcome of specified ventilation flow rate. This is why the ventilated data predictions in Figures 8a and 8b are not at the same cavitations numbers as the natural ventilation cases.) The similarity between the natural and ventilated cavity results are generally affirmed by the simulations, in that these parameters correlate well with each other and with the experimental data provided in Figures 5a and 5b.

Three-Dimensional Natural Cavitation

In order to demonstrate the three-dimensional capability of the method, a model of the hemispherical fore-body configuration studied above was run at numerous angles of attack and a cavitation number of 0.3. A 97x33x65 mesh was utilized (corresponding to the "medium" mesh size discussed in grid studies above). The domain was decomposed into 8 subdomains azimuthally and run on 8 SGI RS10K Octane machines. Parallel efficiencies of 85% were achieved for these problems.

Figure 9 provides sample results for angles of attack of 0.0^o, 2.5^o, 5.0^o and 7.5^o. These plots include pressure contours on the plane of symmetry, sample streamlines and the cavitation bubble shape as identified with an isosurface of $\alpha_l = 0.99$. Several interesting features are observed in the predictions. In particular, the flows are seen to be highly three-dimensional in nature at angle-of-attack. A recirculation zone aft of the bubble, grows with angle of attack. This diminishes the local pressure recovery

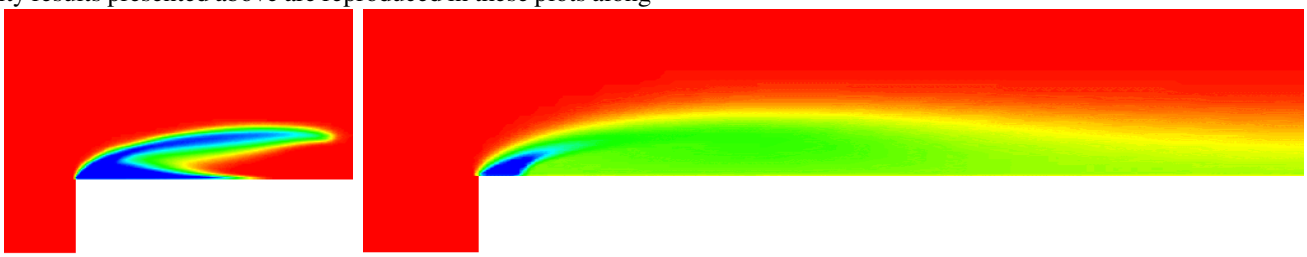

Figure 7. Predicted liquid volume fraction contours for axisymmetric natural and ventilated cavities about a cylindrical configuration with blunt fore-body ($\sigma = 0.4$).

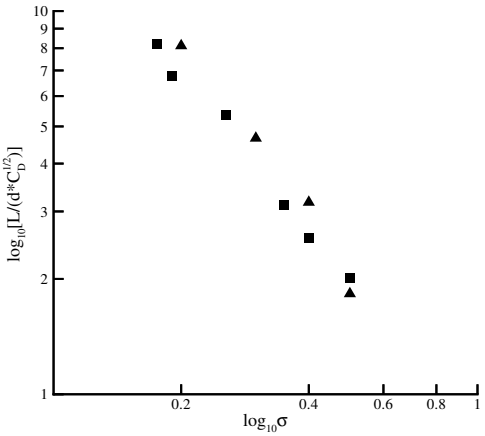

Figure 8a. Comparison of $L/(dC_D^{1/2})$ vs. σ for natural and ventilated cavities about a blunt fore-body.

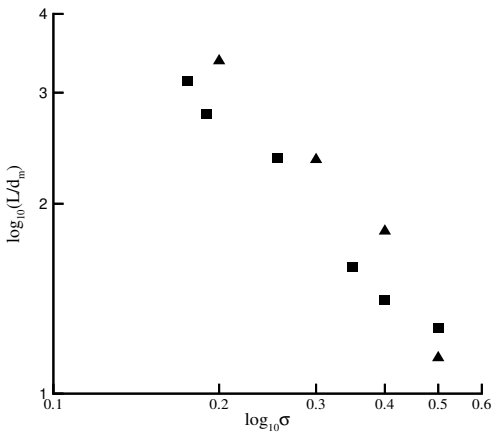

Figure 8b. Comparison of L/d_m vs. σ for natural and ventilated cavities about a blunt fore-body.

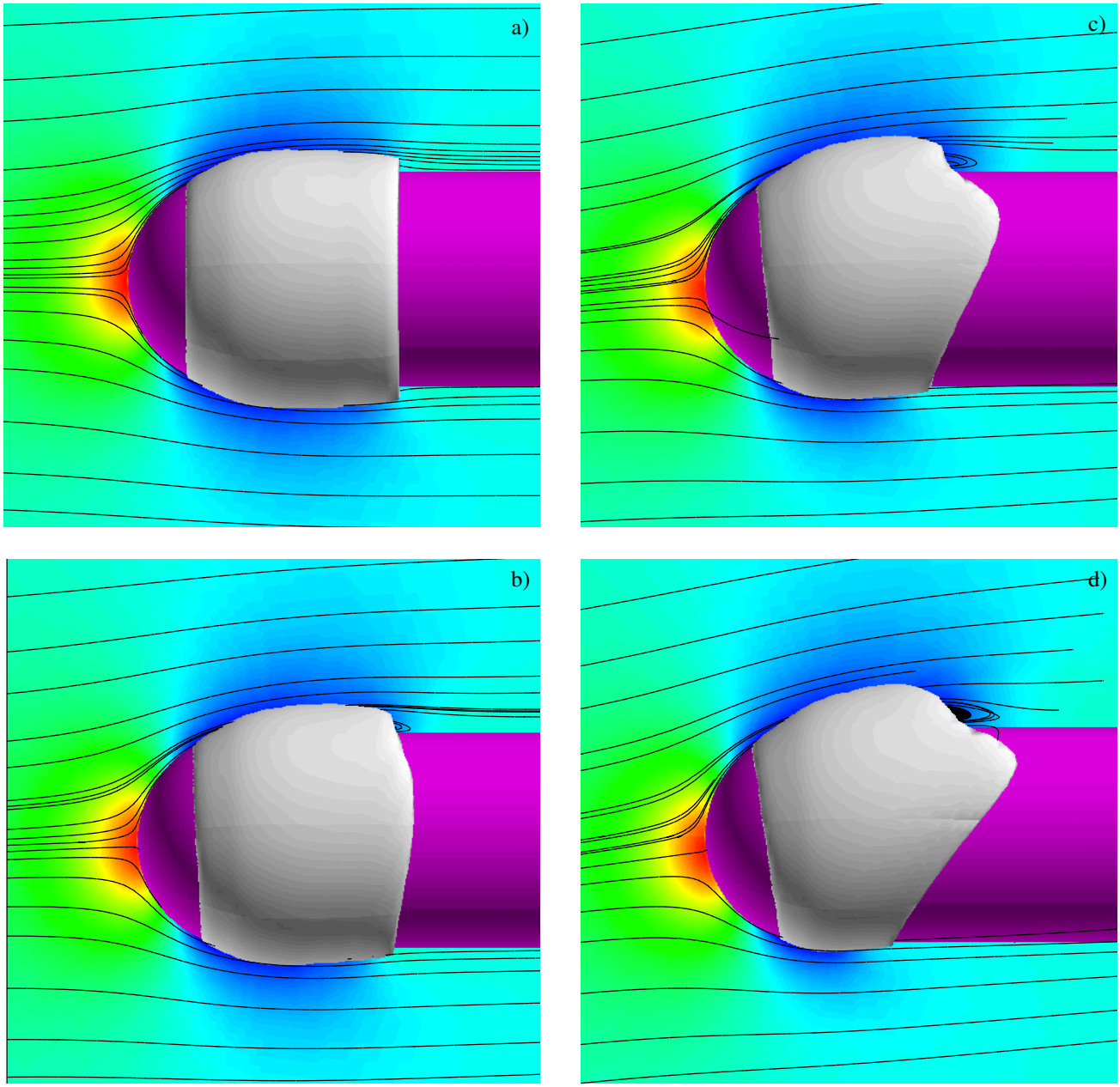

Figure 9. Predicted three-dimensional flow fields with natural cavitation about hemispherical fore-body at several angles of attack. a) α=0.0^o, b) α=2.5^o, c) α=5.0^o, d) α=7.5^o. Flow-field pressure contours, selected streamlines and liquid volume fraction = 0.99 isosurface.

associated with the bubble-induced blockage and this in turn leads to a local collapse of the bubble on the top of the body. Indeed at angle-of-attack the bubble is seen to have its greatest axial extent off of the symmetry plane of the geometry.

Figure 10 shows the convergence history for the $\alpha = 10^o$ case.

At this cavitation number, $\sigma = 0.3$, steady state solutions could be obtained for an angle of attack as high as 15^o. Figure 11 illustrates the predicted bubble shape and complex streamline pattern for this simulation. The bubble shape is highly three-dimensional in nature; it does not close on the pressure side of the body. The streamline pattern is characterized by a large recirculation zone aft of the bubble and significant azimuthally oriented vortical structures.

CONCLUSIONS

A method for analyzing two-phase flows has been presented and applied to natural and ventilated cavitation about a number of external flow configurations. The following conclusions apply:

1) The pressure distributions associated with natural sheet cavitation are well predicted for a cylindrical body with a hemispherical fore-body, across the entire range of cavitation numbers considered.

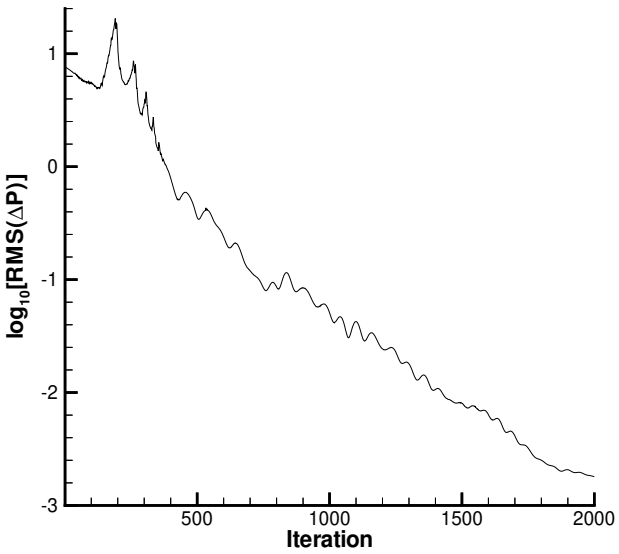

igure 10. Convergence history for three-dimensional simulation of natural cavitation about a cylindrical after-body with hemispherical fore-body, $\sigma = 0.3$, $\alpha = 10^o$.

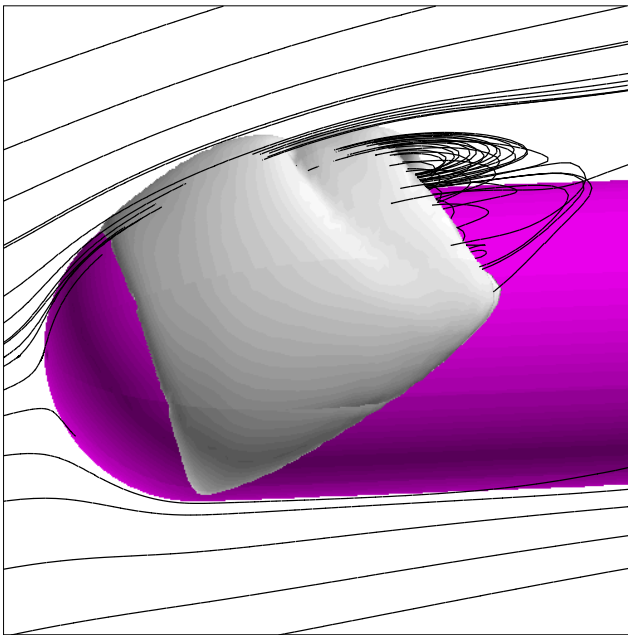

Figure 11. Predicted 3-D flow field with natural cavitation about hemispherical fore-body, $\sigma = 0.3$, $\alpha = 15.0^o$. Selected streamlines and liquid volume fraction = 0.99

2) Weaknesses in the current modeling were observed in the cone and blunt fore-body analyses, due in part to single phase turbulence modeling and in part to the inability to capture more complex off-body cavitation.

3) The method is capable of reproducing the cavitation number dependency of the quantities $L/(dC_D^{1/2})$ and L/d_m.

4) Ventilated cavities are observed to yield similar solutions to natural cavities, as expected.

5) The three-dimensional capability of the method was demonstrated. Significant three-dimensionality was observed for natural cavitation about configurations run at angle of attack.

The authors continue to pursue the present method in the areas of improved physical modeling, algorithm improvement and application to more complex three-dimensional configurations.

ACKNOWLEDGMENTS

This work is supported by the Office of Naval Research, contract # N00014-98-1-0143, with Mr. James Fein as contract monitor. The authors acknowledge Sankaran Venkateswaran and Phil Buelow with whom several conversations benefited the present work.

REFERENCES

1) Chen, Y., Heister, S.D., 1994, “Two-Phase Modeling of Cavitated Flows,” ASME FED-Vol. 190, pp.299-307.
2 Garabedian, P.R., 1958, “Calculation of Axially Symmetric Cavities and Jets,” Pac. J. of Math 6.
3) Grogger, H.A., Alajbegovic, A., 1998, “Calculation of the Cavitating Flow in Venturi Geometries Using Two Fluid Model,” ASME Paper FEDSM 98-5295.
4) Hohenberg, P.C. and Halperin, B.I., 1977, “Theory of Dynamic Critical Phenomena,” Reviews of Modern Physics, Vol. 49, No. 3, pp. 435-479.
5) Kunz, R. F., Boger, D.A., Gibeling, H.J., Govindan, T.R., 1999, “A Preconditioned Navier-Stokes Method for Two-Phase Flows,” AIAA Paper 99-3329, Proc. 14th AIAA CFD Conference.
6) May, A., 1975, “Water Entry and the Cavity-Running Behaviour of Missles,” Naval Sea Systems Command Hydroballistics Advisory Committee Technical Report 75-2.
7) Merkle, C.L., Feng, J., Buelow, P.E.O., 1998, “Computational Modeling of the Dynamics of Sheet Cavitation,” 3rd International Symposium on Cavitation, Grenoble, France.
8) Reichardt, H., 1946, “The Laws of Cavitation Bubbles at Axially Symmetrical Bodies in a Flow,” Ministry of Aircraft Production Volkenrode, MAP-VG, Reports and Translations 766, Office of Naval Research.
9) Rouse, H. and McNown, J. S., 1948, “Cavitation and Pressure Distribution, Head Forms at Zero Angle of Yaw,” Studies in Engineering Bulletin 32, State University of Iowa.
10) Song, C., He, J., 1998, "Numerical Simulation of Cavitating Flows by Single-phase Flow Approach,” 3rd International Symposium on Cavitation, Grenoble, France.
11) Taylor, L. K., Arabshahi, A., Whitfield, D. L., 1995, “Unsteady Three-Dimensional Incompressible Navier-Stokes Computations for a Prolate Spheroid Undergoing Time-Dependent Maneuvers,” AIAA Paper 95-0313.